Journal of Physics: Conference Series

PAPER • OPEN ACCESS

The Biermann catastrophe of numerical MHD

To cite this article: C Graziani *et al* 2016 *J. Phys.: Conf. Ser.* **719** 012018

The Biermann catastrophe of numerical MHD

C Graziani[1], P Tzeferacos, D Lee, D Q Lamb, K Weide, M Fatenejad and J Miller

Flash Center for Computational Science, Department of Astronomy & Astrophysics, University of Chicago, Chicago, IL, 60637

E-mail: [1]`carlo@oddjob.uchicago.edu`

Abstract. The Biermann Battery effect is frequently invoked in cosmic magnetogenesis and studied in High-Energy Density laboratory physics experiments. Unfortunately, direct implementation of the Biermann effect in MHD codes is known to produce unphysical magnetic fields at shocks whose value does not converge with resolution. We show that this convergence breakdown is due to naive discretization, which fails to account for the fact that discretized irrotational vector fields have spurious solenoidal components that grow without bound near a discontinuity. We show that careful consideration of the kinetics of ion viscous shocks leads to a formulation of the Biermann effect that gives rise to a convergent algorithm. We note a novel physical effect a *resistive magnetic precursor* in which Biermann-generated field in the shock "leaks" resistively upstream. The effect appears to be potentially observable in experiments at laser facilities.

1. Introduction

Dynamo theories of proto- and extra-galactic primordial magnetic fields, which endeavor to explain how those fields achieved their current strength and structure, work by amplifying small initial seed fields by means of turbulent plasma motions [1, 2]. However, the induction equation of resistive magnetohydrodynamics (MHD),

$$\frac{\partial \mathbf{B}}{\partial t} = \nabla \times \left\{ \mathbf{u} \times \mathbf{B} - \frac{\eta c^2}{4\pi} \nabla \times \mathbf{B} \right\}, \tag{1}$$

always admits the solution $\mathbf{B}(\mathbf{x}, t) = 0$. This poses a problem for the generation of the required seed fields, as they cannot be created in ideal MHD starting from a field-free state.

There have been several proposals for generating the required seed fields from mechanisms such as primordial phase transitions, or from processes occurring during inflation [3, 4]. The Biermann battery effect [5] provides another popular resolution of this problem [2, 3, 6]. The effect, which arises in consequence of the large difference in the electron and ion mass, is attributable to small-scale charge separation in the plasma. Pressure forces produce much larger accelerations of electrons than of ions, and the relative acceleration of the two components results in charge separation that must be balanced by an electric field

$$\mathbf{E}_B \equiv -(en_e)^{-1} \nabla P_e, \tag{2}$$

where n_e and P_e are the electron number density and pressure, respectively. Since this field is not, in general, irrotational, it can act as a source of magnetic field in the induction equation,

$$\frac{\partial \mathbf{B}}{\partial t} = \nabla \times \left\{ \mathbf{u} \times \mathbf{B} - \frac{\eta c^2}{4\pi} \nabla \times \mathbf{B} + \frac{c}{e n_e} \nabla P_e \right\}, \tag{3}$$

generating a non-zero $\mathbf{B}$ from an initially unmagnetized state.

The Biermann battery effect has been successfully invoked in numerical simulations exploring the generation of seed fields in cosmological ionization fronts [7, 8], protogalaxies [9], and Pop-III star formation [10]. Magnetic field generation by the Biermann mechanism is also of significant interest in direct-drive and indirect-drive inertial confinement fusion, where strong gradients behind the converging shock can lead to dynamically important field strengths [11], and more generally in the field of High-Energy Density Physics, where the effects of field generation [12] and amplification [13] can be examined in a laboratory setting at laser facilities, in experiments where large gradients are produced in strong plasma shocks [14, 15, 16].

Unfortunately, a straightforward implementation of the Biermann effect in finite-volume Eulerian, purely Langrangian, and ALE codes, whether as a split source term or as a flux term, leads to non-convergent results [17]. In symmetric situations such as planar or spherical shocks, where no field should arise, such implementations produce anomalous field generation that grows without bound with resolution [17]. This behavior is observed across a range of different MHD codes (see the discussion of codes in [17]). This is the Biermann catastrophe of numerical MHD. We show below that this failure is intimately related to the failure of such codes to correctly model the structure of the plasma shock.

In a gasdynamic/MHD formulation, where the shocks are modeled as zero-width discontinuities of the flow, the trouble arises from the behavior of the Biermann flux, which is to say from the electric field, Equation (2), in the vicinity of a shock. The gradient ∇P_e, which analytically speaking acquires a Dirac δ component at the shock, is ascribed a numerical magnitude that grows without bound at the shock with increasing resolution. It is this divergence that is connected with failure of MHD codes to correctly predict shock-driven magnetic field generation in supposedly simple test cases, where the correct value of the generated field is zero. The investigation of this failure is one of the central concerns of this article.

In what follows, we appeal to the kinetic theory of the structure of plasma shocks to guide us to an accurate and convergent treatment of the effect in MHD codes. We clarify the origin of the Biermann catastrophe as a numerical effect attributable to the difficulty of discretizing the source term of Equation (2) in the vicinity of a shock. We show that the numerical anomaly can be eliminated by leveraging the continuity of the electron temperature T_e across shocks. Reformulation of the Biermann source term in terms of T_e allows the singularity to be isolated, and the flux of magnetic field due to the Biermann effect to be rewritten in a manifestly finite form suitable for translation into a convergent numerical algorithm.

The Biermann effect is due to electron-ion charge separation, and is sensitive to departure from thermal equilibrium between electrons and ions. Such a departure is precisely what occurs at shocks, so that a correct treatment of the effect at shocks necessarily requires that the disequilibrium be modeled. For this, a 2-temperature plasma model is mandatory. There is no consistent treatment of the Biermann effect at shock in full electron-ion thermal equilibrium.

We also point out a novel and interesting effect associated with the Biermann effect near a shock: A *resistive magnetic precursor* is generated in resistive MHD, wherein magnetic field generated by the Biermann effect in the shock "leaks" resistively into the upstream fluid whose physical extent is proportional to the resistivity. The effect is potentially observable in laboratory conditions at high-intensity laser facilities such as Vulcan, Omega, and NIF. An appropriately-designed experiment at such facilities could currently observe the precursor, providing a clean experimental validation test of the Biermann effect in plasma shocks.

2. The Biermann battery at shocks

We begin by reviewing some essential results from the kinetic theory of shocks in plasmas. The basic theory of the fluid structure of planar shocks in plasmas was set out in [18], while the electromagnetic structure of such shocks was discussed in [19], and more recently in [20]. An extremely lucid presentation of these results may be found in Chapter VII of [21].

The essential ingredients to be imported from the kinetic theory of plasma shocks in order to fashion a working MHD model of the Biermann effect are (1) the loss of thermal equilibrium between electrons and ions at shocks; and (2) the adiabatic behavior of electrons.

As discussed on p.36 of [22], a strong shock disturbs the thermal equilibrium between electrons and ions in a plasma. That equilibrium is maintained by electron-ion collisions, and operates over timescales τ_{ei} that are long compared to the shock-crossing time of a parcel of fluid entering the ion viscous shock in consequence of the large ratio m_i/m_e [23]. As a result, it is essential to describe the fluid in terms of an additional degree of freedom – the electron temperature, T_e – with respect to the usual equilibrium MHD model.

Fortunately, it is unnecessary to model the fluid using new inertial degrees of freedom to describe the electron fluid. A single inertial component for the fluid as a whole gives an adequate description of the fluid structure near the shock, and a completely satisfactory description of the fluid in smooth flow regions, where electron-ion collisions restore local thermal equilibrium [22, 21]. This makes it easier to adapt existing MHD codes to treat the Biermann effect correctly, since it is much easier to add a scalar degree of freedom for T_e than it would be to deal with two velocity fields, one each for the electron fluid and for the ion fluid.

The large ion-to-electron mass ratio, which we recall from the discussion preceding Equation (2) is responsible for the charge separation that produces the Biermann effect, has the further consequence that thermal conductivity due to electron-electron collisions dominates the heat transport in the fluid. At the same time, the forces between electrons and ions as the fluid crosses the ion viscous shock front are effectively dissipation-free, as they are simply electrostatic fields generated by charge separation, and collisional dissipation processes are too slow to act during the shock-crossing timescale.

These observations lead to the conclusion that while the ions undergoing shock compression experience the usual entropy-generating processes, the electrons are compressed *adiabatically* by the electrostatic forces exerted upon them by the ions, and consequently do not suffer entropy increments due to shock compression. The electron entropy is thus a passively-advected scalar, except for the dissipative effect of electron thermal conduction, and for the slow (relative to timescales relevant to the shock) effect of electron-ion collisional equilibration. Electron thermal conduction effectively rules out any sudden change in T_e at the shock, since such a change would produce an enormous restoring heat flux to heal the discontinuity.

The fluid structure that follows from these considerations is of a sudden discontinuous compression of the ions at the shock, accompanied by a smooth increase in T_e, which is continuous throughout the shock (in the Eulerian limit where the shock width tends to zero, T_e acquires a discontinuous derivative in the direction of the shock normal). The electron temperature exhibits a *thermal precursor* that leads the shock. The size λ_T of the precursor region may be calculated by balancing advection against heat diffusion in the shock frame:

$$\lambda_T \approx \frac{\kappa_e}{\rho c_{v,e} D}, \tag{4}$$

where κ_e is the electron thermal conductivity, $c_{v,e}$ is the electron specific heat at constant volume per unit mass, and D is the shock speed [18, 21]. The effect of the precursor region on accretion shocks in galaxy clusters has been recently studied in [24].

The additional degree of freedom represented by T_e must be modeled numerically by adding an equation to the usual equations of compressible MHD. That is, in addition to the usual conservation laws for mass, momentum, and energy, and to the Equation (3) for $\mathbf{B}$, we need to choose a variable whose evolution equation allows us to track T_e. While there are many such variables available (T_e itself, or the ion thermal energy, for example), and while all such evolutions would agree in smooth flow, not all such equations give the correct behavior at shocks. In order to guarantee the nearly-adiabatic behavior of electrons, it is necessary to choose the *specific electron entropy* s_e as our variable, and use the evolution equation

$$\frac{\partial \rho s_e}{\partial t} + \nabla \cdot (\rho \mathbf{u} s_e) = -{T_e}^{-1} \nabla \cdot (-\kappa_e \nabla T_e) + \frac{\rho c_{v,e}}{T_e \tau_{ei}}(T_i - T_e), \tag{5}$$

which expresses the conservation of electron entropy s_e (up to heat conduction and electron-ion heat exchange). As we pointed out above, this is required by the same approximation $m_e/m_i \to 0$ that gives rise to the Biermann effect in the first place.

3. The Biermann Effect At Shocks

By inspection of the Biermann source term in Equation (3) we see that it is proportional to $\nabla n_e \times \nabla P_e$. It follows that field generation by the Biermann effect can only occur if the gradients of n_e and P_e are not aligned. This means that in shocks with planar, cylindrical, or spherical symmetry, the field generation rate is zero. We must therefore treat non-symmetric shock surfaces in order to analyze non-trivial cases of field generation. Accordingly, in this subsection, we set up the basic kinematics of the Biermann effect at general shock surfaces.

To describe the shock surface, we introduce a level function $\Psi(\mathbf{x}, t)$, and use it to define the shock surface $\Psi(\mathbf{x}, t) = 0$. Note that the function Ψ is of no dynamical significance, but is rather simply a mathematical convenience for describing the shock surface. We will assume that the shock is moving in the direction of the normal vector $\mathbf{n} \equiv \nabla\Psi/|\nabla\Psi|$, so that the region $\Psi(\mathbf{x}, t) > 0$ is upstream, whereas the region $\Psi(\mathbf{x}, t) < 0$ is downstream.

We denote the local shock speed along $\mathbf{n}$ by D. By considering the motion of the level surface $\Psi(\mathbf{x}, t) = 0$ it is not difficult to show that

$$D = -\frac{\partial \Psi}{\partial t} / \left|\nabla\Psi\right|. \tag{6}$$

The treatment of shock kinematics is complicated by the fact that, as we have noted, the standard flux term for magnetic field is suspect, because it is not well-defined at a discontinuity. The usual route to the Rankine-Hugoniot shock conditions, in which one balances the fluxes on either side of the shock in the rest frame of the shock, is therefore precluded. We adopt an alternative route that circumvents this difficulty.

To describe a moving MHD discontinuity that coincides with the surface $\Psi(\mathbf{x}, t) = 0$, we will express a field quantity X by the decomposition $X = X_u(\mathbf{x}, t)\Theta(\Psi) + X_d(\mathbf{x}, t)\Theta(-\Psi)$, where X_u and X_d are continuous functions, and where $\Theta(\Psi)$ is a Heaviside step function. After substituting into field equations, we will find some terms proportional to the Dirac distribution $\delta(\Psi)$, resulting from differentiation of the Heaviside functions. We will refer to the collected terms of this form as the "shock part" of the evolution equations. Such terms embody Rankine-Hugoniot jumps, which can thus be efficiently extracted for these non-symmetric shocks. This trick is also useful for deducing hydrodynamic flux terms, as will also be evident below.

It is convenient to reformulate the Biermann source term using the ideal equation of state to replace n_e with T_e, the electron temperature. Assuming an ideal gas equation of state, the reformulated electric field is

$$\mathbf{E}_B \equiv -(k_B/e) T_e \nabla \ln P_e, \tag{7}$$

so that the source term due to the Biermann effect in the induction equation is

$$\left.\frac{\partial \mathbf{B}}{\partial t}\right|_B = (c k_B/e) \nabla T_e \times \nabla \ln P_e. \tag{8}$$

An important reason for this reformulation is that as we saw in §2, in the presence of electron thermal conduction, T_e *is continuous at the shock*, whereas n_e is not [18, 21]). As we saw, the continuity of T_e is a consequence of the high mobility of electrons relative to ions, and is therefore part and parcel of the same approximation that led to the Biermann source term (Equation 2) in the first place. It is central to the developments that follow.

Using this reformulation, we may write for the induction equation

$$\frac{\partial \mathbf{B}}{\partial t} = \nabla \cdot \{\mathbf{Bu} - \mathbf{uB}\} + \frac{ck_B}{e} \nabla T_e \times \nabla \ln P_e. \tag{9}$$

Plugging in the discontinuous form for the various field variables, and respecting the continuity of T_e and of the normal magnetic field, we obtain

$$\begin{aligned}
\nabla \ln P_e &= \Theta(\Psi)\nabla \ln P_{e,u} + \Theta(-\Psi)\nabla \ln P_{e,d} + [\ln P_e]_d^u \, \delta(\Psi)\nabla\Psi & (10)\\
\nabla T_e &= \Theta(\Psi)\nabla T_{e,u} + \Theta(-\Psi)\nabla T_{e,d} & (11)\\
\mathbf{B} &= B_n \mathbf{n} + \mathbf{B}_{Tu}\Theta(\Psi) + \mathbf{B}_{Td}\Theta(-\Psi) & (12)\\
\mathbf{u} &= \mathbf{u}_u\Theta(\Psi) + \mathbf{u}_d\Theta(-\Psi) & (13)
\end{aligned}$$

After plugging Equations (10-13) and Equation (6) into Equation (9) and isolating the Dirac δ-function term in the resulting equation, we obtain the corrected Rankine-Hugoniot equation

$$[(D - u_n)\mathbf{B}_T]_d^u + B_n [\mathbf{u}_T]_d^u + \frac{ck_B}{e} \nabla T_e \times \mathbf{n} [\ln P_e]_d^u = 0. \tag{14}$$

In this equation, $\mathbf{u}_T$ and $\mathbf{B}_T$ are respectively the fluid velocity and magnetic field component transverse to the shock, while u_n and B_n are the longitudinal velocity and field components. The notation $[\ldots]_d^u$ means the difference of the upstream and downstream values at the shock location. The first two terms in Equation (14) comprise the usual jump condition for the induction equation (see Chapter 7 of [25] for example). The final term is the contribution to the jump condition from the Biermann effect, which, in consequence of the continuity of T_e is seen to produce a finite, well-defined discontinuity at the shock.

We conclude from the above development that the Biermann source term is mathematically well-defined even at weak solution discontinuities, and yields definite finite predictions to which a properly designed numerical algorithm should be expected to converge.

4. Correcting the algorithm

The origin of the Biermann catastrophe may be diagnosed by means of a calculation described in [26]. It can be shown that even in simulations in which one expects that $\nabla P_e \propto \nabla n_e$, the discrete representation of the curl of the "irrotational" Biermann electric field, $\nabla \times \left(n_e{}^{-1} \nabla P_e\right)$, diverges as $\mathcal{O}(\Delta^{-1})$ at a discontinuity. Consequently, at discontinuities, the "naively discretized" Biermann electric field grows *spurious solenoidal behavior* that diverges with increasing resolution.

To design a better algorithm we need a flux of $\mathbf{B}$ along $\mathbf{n}$ that is well-behaved at shocks, unlike the flux $c\mathbf{n} \times \mathbf{E}_B = -(ck_B/e)T_e \mathbf{n} \times \nabla \ln P_e$ that would be inferred from the naive Biermann term. To obtain such a flux, we can reverse the usual logic of the Rankine-Hugoniot jump conditions: instead of deriving the jump from the flux, we can infer the flux from the jump!

In terms of the flux $\mathbf{F}_\Phi$ of a generic field variable Φ, the Rankine-Hugoniot condition at a shock traveling with speed D along the unit normal $\mathbf{n}$ is given by

$$D \times [\Phi]_d^u = [\mathbf{n} \cdot \mathbf{F}_\Phi]_d^u \, . \tag{15}$$

Comparing this expression to the corrected Rankine-Hugoniot jump condition for $\mathbf{B}$ given in Equation (14) we may immediately infer the corrected flux of $\mathbf{B}$:

$$\mathbf{n} \cdot \mathbf{F_B} = (\mathbf{n} \cdot \mathbf{u})\mathbf{B}_T - (\mathbf{n} \cdot \mathbf{B})\mathbf{u}_T + \frac{ck_B}{e} \ln P_e \mathbf{n} \times \nabla T_e. \tag{16}$$

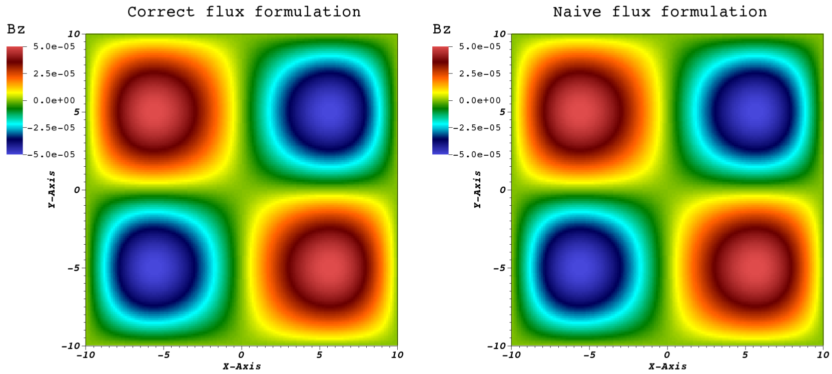

Figure 1. Smooth test in a cartesian box. In both panels we show the magnetic field generated after one computational step for the correct and naive flux formulations (left and right respectively). Both methods recover the analytical solution of Equation (17).

The third term in this expression is the correction due to the Biermann term, which is manifestly well-defined at discontinuities. From the form of Equation (16), only the tangential components of **B** are subject to change according to the Rankine-Hugoniot condition, as expected.

Discretization of the Biermann effect based on this flux expression is convergent *so long as the mesh resolves the scales on which T_e is continuous.* The scale at which T_e is continuous is the scale length λ_T of the electron thermal conduction precursor region [18, 19, 21], discussed in §2. This length scale is characteristic of the variation of temperature perpendicular to the shock; however, it is also the length scale over which heat diffuses transversely during the time required for the shock to travel a distance λ_T (and hence traverse its own thermal precursor). It is therefore the scale to be resolved in order for the discretization of Equation (16) to converge. At coarser resolutions, T_e appears as discontinuous at shocks as all the other fluid variables, and the discretization discussed here will not yield converged results for **B**. Only as the thermal precursor zone is resolved can convergence be expected.

5. Numerical Verification

5.1. Implementation Using the FLASH Code

We have implemented the corrected Biermann Effect algorithm within the publically-available FLASH hydrodynamic simulation framework [16, 27, 28]. FLASH is a modular and extensible multiphysics scientific simulation software package that has been widely used for reactive compressible flows typical of astrophysical situations, High-Energy Density Physics (HEDP) applications, cosmology, computational fluid dynamics, and fluid–structure interactions. In particular, FLASH makes available both a 2-temperature single-fluid model and resistive MHD, which makes it an ideal platform for testing the proposed algorithm.

We incorporated the new flux term represented by Equation (16) into the FLASH MHD solver. FLASH also supports electron entropy advection, Equation (5), with the standard Sackur-Tetrode equation for entropy (see, for example, p. 77 of [29]) implemented in the EOS.

5.2. Smooth flow

The first test problem considers a smooth electron density and pressure configuration for which the analytic calculation of the magnetic field generation due to the Biermann Effect is trivial. We employ this test to verify the implementations of the naive and correct flux formulations, which should both be able to recover the analytic solution. This non-dimensional 2D problem

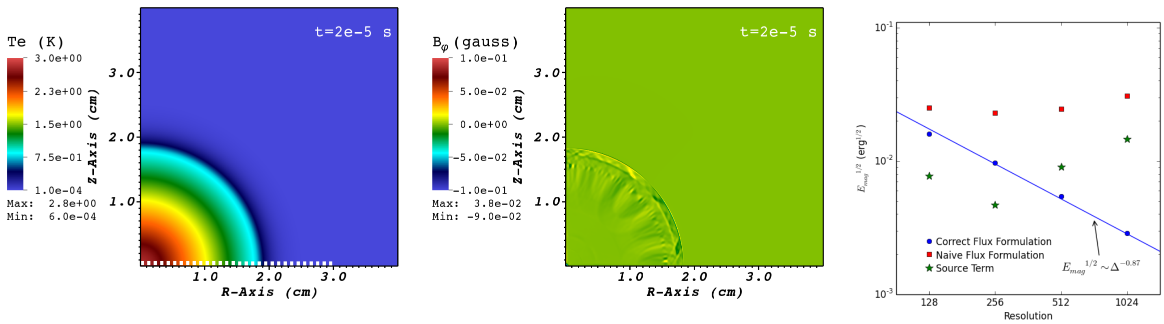

Figure 2. Null test using a spherical shock. Left panel: electron temperature distribution for a near-Sedov explosion. Middle panel: B_ϕ due to numerical noise. Right panel: Total magnetic energy as a function of simulation resolution, showing convergence of the new algorithm and convergence failure of the old source term and flux term algorithms.

is drawn from [30] and assumes an initial condition of $\mathbf{B} = 0$, $\mathbf{u} = 0$, $n_e = n_0 + n_1\, cos(k_x\, x)$, and $P_e = P_0 + P_1\, cos(k_y\, y)$, where $k_x = k_y = \pi/10$, $n_0 = P_0 = 1$, and $n_1 = P_1 = 0.1$. The cartesian domain spans from -10 to 10 in x and y, with periodic boundary conditions on both directions. The resulting magnetic field generation rate in the z direction will then be

$$\frac{\partial B_z}{\partial t} = -\frac{k_x\, k_y\, n_1\, P_1\, sin(k_x\, x)\, sin(k_y\, y)}{[n_0 + n_1\, cos(k_x\, x)]^2} \tag{17}$$

As in [30], we use a resolution of $[160 \times 160]$ points and take one step, $\Delta t = 0.05$, to recover the analytic solution for both implementations. Both results agree with the analytic solution (Figure 1) within an error of $\sim 2 \times 10^{-8}$ (see also figure 6 in [30]).

5.3. Shocked flow

In the simulations that follow, we assume fully-ionized Hydrogen – $A = 1$, $Z = 1$, adiabatic index $\gamma = 5/3$, $c_{v,e} = \frac{3}{2} k_B N_A$, where N_A is Avogadro's number and k_B is Boltzmann's constant. Simulations are conducted in cylindrical coordinates, assuming azimuthal symmetry, and are therefore 2-dimensional. In addition, we impose a reflection boundary on the R-axis (where R is perpendicular distance from axis of rotational symmetry, which is to say, R is the cylindrical radius) so that the domain represents a hemisphere of a solution with reflection symmetry about that axis. In every case, the domain is 4 cm radius cylinder that extends 4 cm in the z direction from the R axis. The boundary conditions at $R = 4$ cm and at $z = 4$ cm are outflow. Magnetic fields are always azimuthal in these verification tests – since the gradients of T_e and P_e are always in the $R - z$ plane the Biermann effect only generates non-zero field along the azimuthal direction. These simulations are described in greater detail in [26].

It is not easy to construct a non-trivial analytic verification solution of a plasma shock magnetized by the Biermann effect. However, a trivial solution may be constructed by imposing symmetry requirements that align the gradients ∇P_e and ∇T_e, thus guaranteeing zero field generation. We use a spherical Sedov-like explosion as an example of such a test. This is in fact the test that revealed the Biermann catastrophe in the first place [17].

The results of this study are shown in Figure 2. The left panel shows the electron temperature T_e and the middle panel shows the magnetic field strength generated by the corrected treatment using the flux in Equation (16). We see spurious non-zero field due to numerical noise. However,

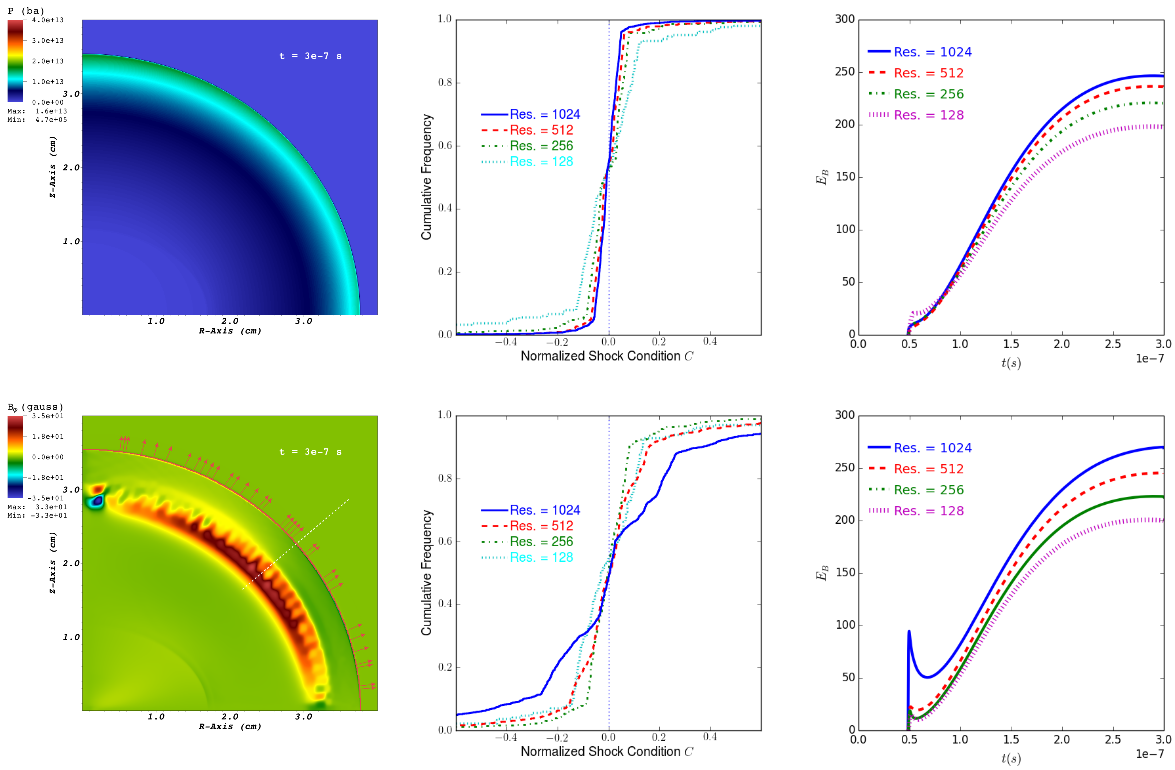

Figure 3. Results for an ellipsoidal shock. Top left: pressure distribution; Bottom Left: magnetic field distribution. The solid red line displays the location of the shock, while the red arrows display the direction of the shock normal; Middle Panels: Cumulative distribution of the normalized magnetic shock condition C, defined by Equation (21), evaluated at points along the shock surface, for four different resolutions, illustrating convergence to the correct jump condition for the corrected algorithm (top panel), and convergence failure for the naive algorithm (bottom panel); Right Panels: Total magnetic energy as a function of simulation time for the four resolutions studied, for the corrected algorithm (top panel) and for the naive algorithm (bottom panel).

the right panel shows that this field is converging to zero with increasing resolution. This figure displays the square-root of the total magnetic energy in the domain. Since the analytic solution for the magnetic field strength is zero everywhere, this quantity functions as an un-normalized L^2-norm of the difference between the analytic and numerical solutions. The blue circles show the convergence with resolution of the correct formulation. This convergence behavior is in contrast to the behavior of two algorithms that use the uncorrected Biermann term (a flux-based formulation, and a source term), which fail altogether to converge.

Next we exhibit simulations designed to produce non-zero values of the magnetic field strength. We start an ellipsoidal shock surface, obtained by distorting the spherical Sedov solution. The state of the shock after a period during which magnetic field is generated is illustrated by the pressure colormap plot in the top-left panel of Figure 3. The lower-left panel of Figure 3 shows the magnetic field intensity generated according to the corrected flux, ranging into the tens of Gauss. The solid red line in the figure shows the shock location, while the red arrows display the shock unit normal vector.

We do not have an analytical solution for the magnetic field distribution to compare to the output of these simulations. We do, however, have the relation between shock quantities expressed by Equation (14), which determines the jump condition for **B**. By locating points adjoining the shock, and computing the local shock velocity at those points, we can then verify that Equation (14) in fact obtains, to some accuracy limited by the numerical approximation.

To perform this verification, we first locate cells adjoining the shock by the method described in the Appendix of [26], which yields a 1-cell wide shock surface by fitting the mass, momentum, and energy Rankine-Hugoniot conditions to the neighboring data, using a speed-of-sound weighted inner-product on the state space, and treating the shock speed D as a free fit parameter. The fitted shock speed is then used in the verification of Equation (14).

In the absence of normal component field B_n, Equation (14) becomes

$$(D-u_d)B_d-(D-u_u)B_u+\frac{ck_B}{e}\left(n_z\frac{\partial T_e}{\partial R}-n_R\frac{\partial T_e}{\partial z}\right)[\ln P_{e,d}-\ln P_{e,u}]\equiv a_d-a_u+b_d-b_u=0, \quad (18)$$

where we've defined "Advection" terms $a_{d,u}$ and "Biermann" terms $b_{d,u}$ by

$$a_{d,u} \equiv (D-u_{d,u})B_{d,u} \quad (19)$$

$$b_{d,u} \equiv \frac{ck_B}{e}\left(n_z\frac{\partial T_e}{\partial R}-n_R\frac{\partial T_e}{\partial z}\right)\ln P_{d,u} \quad (20)$$

The sum of terms in Equation (18) is required to be zero. In a discretized numerical PDE integration, this really means that the terms must cancel up to some truncation or rounding precision, which is expressed relative to the largest of the magnitudes in play. We therefore define the "shock condition parameter" C by

$$C \equiv \frac{a_d-a_u+b_d-b_u}{\max(|a_d|,|a_u|,|b_d|,|b_u|)}. \quad (21)$$

We calculate the value of C at cells along the shock front, at each of our four resolution levels, for both the correct flux and the "naive" flux implementations. At the highest resolution (1024×1024) the electron precursor length is spanned by about 50 cells, while at the lowest resolution (128×128) it is only spanned by about 6 cells. We therefore expect substantial improvement in the computation of field generation as resolution is progressively refined.

We display cumulative distributions of C for corrected and "naive" flux implementations in the middle panels of Figure 3. It is evident from these figures that the distribution of C is in fact centered near zero for both flux implementations. The width of the distributions behave very differently, however. In the case of the correct Biermann flux implementation, the distributions get narrower with each refinement of resolution – the steepening of the cumulative profile shows that RMS deviations of C from zero shrink progressively with increasing resolution. This provides some evidence of convergence with resolution to the expected result. In the case of the naive flux implementation, there is no such evidence of convergence.

The right panels of Figure 3 show the evolution of total magnetic energy in the domain as a function of time, for the different resolutions and for the two flux implementations. The correct flux implementation appears to be converging (although not in any strong sense converged) by this measure, even at late time, whereas any evidence of convergence in magnetic field energy is simply lacking for the naive flux implementation.

6. New Physics: The Resistive Magnetic Precursor

Recall the physical basis for the electron conduction shock precursor: a balance of heat diffusion out of the shock and heat advection into the shock, in the presence of impulsive heating at the shock. A similar effect occurs for **B** in the presence of finite resistivity η: the balance of magnetic

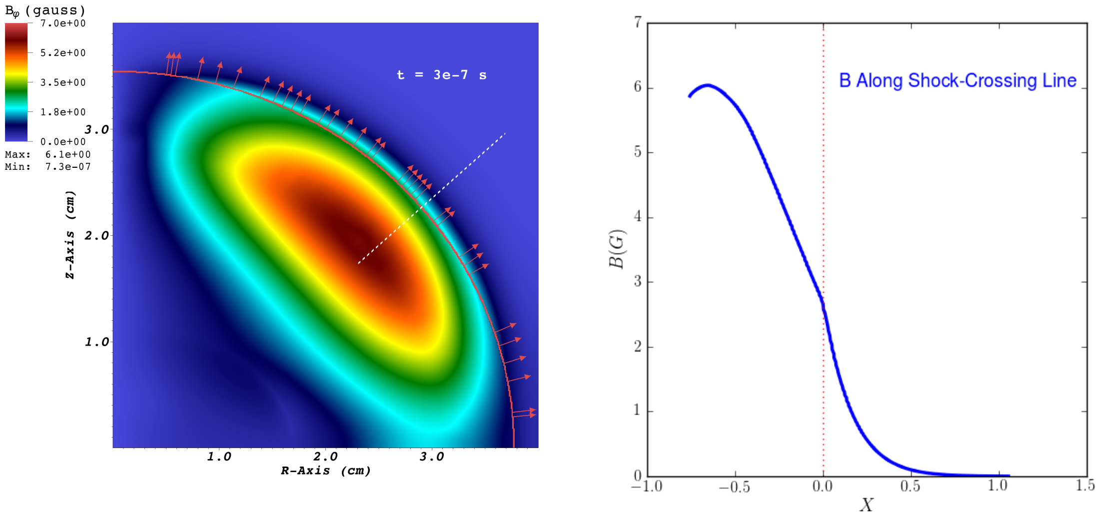

Figure 4. Left Panel: Magnetic field distribution due to passage of shock, in the presence of finite resistivity. The simulation differs from the one shown in Figure 3 only by the presence of non-zero resistivity. The solid red line shows the location of the shock, while the vectors represent the unit normal to the shock. The magnetic precursor can be clearly seen ahead of the shock surface. The white dashed shock-crossing line illustrates the location of the data displayed in the right panel. Right Panel: Magnetic field strength magnitude along the white dashed shock-crossing line shown in the left panel. The position of the shock is shown by the vertical solid red line. The predicted exponential decay of the precursor is evident.

diffusion out of the shock with magnetic advection into the shock in the presence of impulsive magnetogeneration by the BBT at the shock gives rise to a *resistive magnetic shock precursor*.

As shown in [26], the precursor is exponential, with a skin depth $\lambda_B = \frac{c^2\eta}{4\pi D}$. Assuming Spitzer-type diffusion, λ_B scales as follows:

$$\lambda_B = 16.4\,\mathrm{cm} \times Z \times \frac{\ln\Lambda}{10} \times \left(\frac{D}{10^6\,\mathrm{cm\,s^{-1}}}\right)^{-1} \times \left(\frac{k_B T_e}{1\mathrm{eV}}\right)^{-3/2}$$

The scales chosen here are not atypical of the conditions that can be created in a plasma at a large laser facility. Potentially this effect could be the basis of an HEDP validation experiment.

We confirm the presence of this precursor using simulations that maintain the simulation parameters of the ellipsoidal shock described in the previous section, but also turn on the resistivity η to a finite positive value chosen to yield an easily-discernible precursor

The left panel of Figure 4 shows the distribution of magnetic field strength across the domain. The shock location is shown by the solid red line, and the superposed vectors indicate the shock-normal direction. The magnetic field is evidently smoothed out by the resistivity, as can be seen by a direct comparison with the bottom-left panel of Figure 3. The precursor is evident in this figure, as the substantial amount of magnetic field that has "leaked" ahead of the shock.

The diagonal white dashed shock-crossing in the left panel of Figure 4 illustrates the line along which data was extracted to produce the right panel of Figure 4. This figure shows the magnetic field values plotted along that line. The vertical solid red line at $X = 0$ marks the location of the shock. The exponential decay of the field is easily visible in this figure.

References

[1] Kronberg P P 1994 *Reports on Progress in Physics* **57** 325 URL `http://stacks.iop.org/0034-4885/57/i=4/a=001`
[2] Kulsrud R M and Zweibel E G 2008 *Reports on Progress in Physics* **71** 046901 URL `http://stacks.iop.org/0034-4885/71/i=4/a=046901`
[3] Widrow L M 2002 *Reviews of Modern Physics* **74** 775–823 (*Preprint* `astro-ph/0207240`)
[4] Widrow L M, Ryu D, Schleicher D R G, Subramanian K, Tsagas C G and Treumann R A 2012 *Space Sci. Rev.* **166** 37–70 (*Preprint* `1109.4052`)
[5] Biermann L 1950 *Zeitschrift Naturforschung Teil A* **5** 65
[6] Kulsrud R M, Cen R, Ostriker J P and Ryu D 1997 *The Astrophysical Journal* **480** 481 URL `http://stacks.iop.org/0004-637X/480/i=2/a=481`
[7] Subramanian K, Narasimha D and Chitre S M 1994 *MNRAS* **271** L15
[8] Gnedin N Y, Ferrara A and Zweibel E G 2000 *The Astrophysical Journal* **539** 505 URL `http://stacks.iop.org/0004-637X/539/i=2/a=505`
[9] Davies G and Widrow L M 2000 *The Astrophysical Journal* **540** 755 URL `http://stacks.iop.org/0004-637X/540/i=2/a=755`
[10] Xu H, OShea B W, Collins D C, Norman M L, Li H and Li S 2008 *The Astrophysical Journal Letters* **688** L57 URL `http://stacks.iop.org/1538-4357/688/i=2/a=L57`
[11] Srinivasan B and Tang X Z 2013 *Physics of Plasmas (1994-present)* **20** 056307
[12] Gregori G, Ravasio A, Murphy C D, Schaar K, Baird A, Bell A R, Benuzzi-Mounaix A, Bingham R, Constantin C, Drake R P, Edwards M, Everson E T, Gregory C D, Kuramitsu Y, Lau W, Mithen J, Niemann C, Park H S, Remington B A, Reville B, Robinson A P L, Ryutov D D, Sakawa Y, Yang S, Woolsey N C, Koenig M and Miniati F 2012 *Nature* **481** 480–483
[13] Meinecke J, Doyle H W, Miniati F, Bell A R, Bingham R, Crowston R, Drake R P, Fatenejad M, Koenig M, Kuramitsu Y, C Kuranz C, Lamb D Q, Lee D, MacDonald M J, Murphy C D, Park H S, Pelka A, Ravasio A, Sakawa Y, Schekochihin A A, Scopatz A, Tzeferacos P, Wan W C, Woolsey N C, Yurchak R, Reville B and Gregori G 2014 *Nature Physics* **10** 520–524
[14] Fryxell B, Kuranz C, Drake R, Grosskopf M, Budde A, Plewa T, Hearn N, Hansen J, Miles A and Knauer J 2010 *High Energy Density Physics* **6** 162–165
[15] Tzeferacos P, Fatenejad M, Flocke N, Gregori G, Lamb D, Lee D, Meinecke J, Scopatz A and Weide K 2012 *High Energy Density Physics* **8** 322–328
[16] Tzeferacos P, Fatenejad M, Flocke N, Graziani C, Gregori G, Lamb D, Lee D, Meinecke J, Scopatz A and Weide K 2015 *High Energy Density Physics* **17, Part A** 24 – 31
[17] Fatenejad M, Bell A, Benuzzi-Mounaix A, Crowston R, Drake R, Flocke N, Gregori G, Koenig M, Krauland C, Lamb D, Lee D, Marques J, Meinecke J, Miniati F, Murphy C, Park H S, Pelka A, Ravasio A, Remington B, Reville B, Scopatz A, Tzeferacos P, Weide K, Woolsey N, Young R and Yurchak R 2013 *High Energy Density Physics* **9** 172 – 177 ISSN 1574-1818 URL `http://www.sciencedirect.com/science/article/pii/S1574181812001280`
[18] Shafranov V D 1957 *Soviet Physics JETP* **5** 1183–1188
[19] Jaffrin M and Probstein R 1964 *Physics of Fluids* **7** 1658
[20] Amendt P, Milovich J, Wilks S, Li C, Petrasso R and Séguin F 2009 *Plasma Physics and Controlled Fusion* **51** 124048
[21] Zel'dovich, YB and Raizer, YP 2002 *Physics of shock waves and high-temperature hydrodynamic phenomena* (Dover Pubns)
[22] Drake R 2006 *High-Energy-Density Physics: Fundamentals, Inertial Fusion, and Experimental Astrophysics* High pressure shock compression of condensed matter (Springer) ISBN 9783540293149 URL `http://books.google.com/books?id=P-3OeLJZN1YC`
[23] Spitzer L 1962 *Physics of Fully Ionized Gases ... Second Revised Edition* [Interscience Tracts on Physics and Astronomy. no. 3.] (New York, London) URL `http://books.google.com/books?id=06okMwEACAAJ`
[24] Smith B, O'Shea B W, Voit G M, Ventimiglia D and Skillman S W 2013 *ApJ* **778** 152
[25] Gurnett D and Bhattacharjee A 2005 *Introduction to Plasma Physics: With Space and Laboratory Applications* (Cambridge University Press) ISBN 9780521364836 URL `http://books.google.com/books?id=VcueZlunrbcC`
[26] Graziani C, Tzeferacos P, Lee D, Lamb D Q, Weide K, Fatenejad M and Miller J 2015 *The Astrophysical Journal* **802** 43
[27] Fryxell B, Olson K, Ricker P, Timmes F X, Zingale M, Lamb D Q, MacNeice P, Rosner R, Truran J W and Tufo H 2000 *ApJS* **131** 273–334
[28] Dubey A, Antypas K, Ganapathy M K, Reid L B, Riley K, Sheeler D, Siegel A and Weide K 2009 *Parallel Computing* **35** 512–522

[29] Kittel C and Kroemer H 1980 *Thermal physics* (Macmillan)
[30] Tóth G, Van der Holst B, Sokolov I V, De Zeeuw D L, Gombosi T I, Fang F, Manchester W B, Meng X, Najib D, Powell K G *et al.* 2012 *Journal of Computational Physics* **231** 870–903